



RESEARCH ARTICLE

10.1002/2013JF003017

Key Points:

- Simulated brightness temperature biases minimized by grain scaling factors
- Sub-Arctic stratigraphic variability required distributions of simulations
- Three-layer stratigraphic representation reduced bias to about 50% of one-layer

Correspondence to:

N. Rutter,
nick.rutter@northumbria.ac.uk

Citation:

Rutter, N., M. Sandells, C. Derksen, P. Toose, A. Royer, B. Montpetit, A. Langlois, J. Lemmetyinen, and J. Pulliainen (2014), Snow stratigraphic heterogeneity within ground-based passive microwave radiometer footprints: Implications for emission modeling, *J. Geophys. Res. Earth Surf.*, 119, 550–565, doi:10.1002/2013JF003017.

Received 22 OCT 2013

Accepted 7 FEB 2014

Accepted article online 12 FEB 2014

Published online 13 MAR 2014

Snow stratigraphic heterogeneity within ground-based passive microwave radiometer footprints: Implications for emission modeling

Nick Rutter¹, Mel Sandells², Chris Derksen³, Peter Toose³, Alain Royer⁴, Benoit Montpetit⁴, Alex Langlois⁴, Juha Lemmetyinen⁵, and Jouni Pulliainen⁵

¹Department of Geography, Northumbria University, Newcastle upon Tyne, UK, ²NCEO, University of Reading, Reading, UK, ³Environment Canada, Toronto, Ontario, Canada, ⁴Centre d'Applications et de Recherches en Télédétection, Université de Sherbrooke, Sherbrooke, Quebec, Canada, ⁵Finnish Meteorological Institute, Helsinki, Finland

Abstract Two-dimensional measurements of snowpack properties (stratigraphic layering, density, grain size, and temperature) were used as inputs to the multilayer Helsinki University of Technology (HUT) microwave emission model at a centimeter-scale horizontal resolution, across a 4.5 m transect of ground-based passive microwave radiometer footprints near Churchill, Manitoba, Canada. Snowpack stratigraphy was complex (between six and eight layers) with only three layers extending continuously throughout the length of the transect. Distributions of one-dimensional simulations, accurately representing complex stratigraphic layering, were evaluated using measured brightness temperatures. Large biases (36 to 68 K) between simulated and measured brightness temperatures were minimized (−0.5 to 0.6 K), within measurement accuracy, through application of grain scaling factors (2.6 to 5.3) at different combinations of frequencies, polarizations, and model extinction coefficients. Grain scaling factors compensated for uncertainty relating optical specific surface area to HUT effective grain size inputs and quantified relative differences in scattering and absorption properties of various extinction coefficients. The HUT model required accurate representation of ice lenses, particularly at horizontal polarization, and large grain scaling factors highlighted the need to consider microstructure beyond the size of individual grains. As variability of extinction coefficients was strongly influenced by the proportion of large (hoar) grains in a vertical profile, it is important to consider simulations from distributions of one-dimensional profiles rather than single profiles, especially in sub-Arctic snowpacks where stratigraphic variability can be high. Model sensitivity experiments suggested that the level of error in field measurements and the new methodological framework used to apply them in a snow emission model were satisfactory. Layer amalgamation showed that a three-layer representation of snowpack stratigraphy reduced the bias of a one-layer representation by about 50%.

1. Introduction

Reliable estimates of snow water equivalent (SWE) are crucial to our understanding of the energy and water balance from global to catchment scales. In particular, knowledge of the magnitude and variability in snow mass and snow cover has important hydrological implications for global water movement and direct impact on human activities, both in terms of maximization of a resource, e.g., irrigation [Barnett *et al.*, 2005] and mitigation of flooding risks [Payne *et al.*, 2004]. However, direct measurements of SWE are sparse [Brown, 2000; Brown and Braaten, 1998], especially with increasing latitude and decreasing proximity to populated areas. Attempts to simulate SWE spatially often suffer from a similar sparseness of meteorological stations, relying instead on remotely sensed measurements to constrain simulations [Cline *et al.*, 1998; Fletcher *et al.*, 2012; Homan *et al.*, 2011; Molotch and Margulis, 2008]. Differences in instrumentation that provide model driving data, e.g., measurement of precipitation [Yang *et al.*, 1999], also introduce uncertainty in simulations. Errors resulting from interpolation of SWE between such sparse point networks [Takala *et al.*, 2011] means that in many seasonally snow-covered areas of the world, remote sensing is the most practical method for near-real-time monitoring of snow mass distribution.

Current operational satellite data products of snow water equivalent (SWE) are produced from passive microwave measurements with a 25 × 25 km resolution [Kelly, 2009; Tedesco *et al.*, 2004]. Such data products are derived from native satellite footprints described in Kelly [2009] as having instantaneous fields of view at 19 GHz of 28 × 16 km (AMSR-E) or 69 × 43 km (SMM/I), and at 37 GHz of 14 × 8 km (AMSR-E) or 37 × 29 km

This is an open access article under the terms of the Creative Commons Attribution-NonCommercial-NoDerivs License, which permits use and distribution in any medium, provided the original work is properly cited, the use is non-commercial and no modifications or adaptations are made.

(SMM/I). Within these horizontal extents, footprints integrate a huge amount of complexity in land cover (nonvegetated land, lakes, and forests) and snowpack properties such as SWE, grain size, ice lenses, and crusts [Derksen *et al.*, 2005; Kurvonen and Hallikainen, 1997; Lemmetyinen *et al.*, 2009]. Differentiating the influence of subfoot print land cover types (e.g., different forest types and clearings) to account for their characteristic emission and scattering properties is possible by considering the fractional subgrid land cover fractions [Derksen *et al.*, 2003]. However, it is much harder to differentiate physical properties of snow at the subsatellite footprint scale. This is particularly problematic for empirical algorithms because errors are amplified when snow properties deviate from “typical” conditions [e.g., Chang *et al.*, 1987; Kelly *et al.*, 2003]. Forward radiative transfer models used to estimate snow mass from brightness temperatures [e.g., Pulliainen *et al.*, 1999; Wiesmann and Matzler, 1999] are also highly sensitive to variability in snow properties, especially grain size and layering [Durand *et al.*, 2008; Grody, 2008; Harlow and Essery, 2012; Kontu and Pulliainen, 2010; Tedesco *et al.*, 2006].

Acquiring enough in situ measurements of snowpack properties to capture the spatial variability of snow within a satellite footprint sufficiently is challenging. Very few experimental campaigns [e.g., Elder *et al.*, 2009] have collected sufficient, simultaneous snow pit measurements across a wide enough spatial extent to allow direct comparison with satellite brightness temperatures. However, even in high-quality data sets such as those presented by Elder *et al.* [2009], measurements tend to be proximate to road or trail networks creating a spatially uneven distribution of measurements throughout the satellite pixel [Davenport *et al.*, 2012]. Consequently, uncertainty still exists whether or not snow pit measurements adequately captured the variability of snowpack properties throughout the footprint.

Even if snow pits are numerous and well-distributed, further uncertainties are introduced through the measurement of grain size, a proxy for microstructure, and the use of this measurement at optical wavelengths in microwave emission models. While standard field techniques exist for measurement of grain size of snow by placing snow samples on a millimeter-graded grid [Fierz *et al.*, 2009], manual measurements of this kind are prone to subjectivity, especially between observers, which can lead to unsatisfying comparability of results [Derksen *et al.*, 2012]. More objective in situ methods of measuring snow grain size (also referred to as texture or microstructure) in optical wavelengths [Grenfell and Warren, 1999] can be obtained using near-infrared and shortwave infrared photography [Langlois *et al.*, 2010; Matzl and Schneebeli, 2006; Montpetit *et al.*, 2012], integrating lasers [Gallet *et al.*, 2009; Picard *et al.*, 2009], methane adsorption [Domine *et al.*, 2001], and contact spectroscopy [Painter *et al.*, 2007]. Measurement of correlation length [Mätzler, 2002], another metric describing snow microstructure, can be made either directly using X-ray tomography [Freitag *et al.*, 2004; Schneebeli, 2004] or indirectly using either a micropenetrator [Proksch *et al.*, 2012] or near-infrared photography [Touret *et al.*, 2008] using established relationships [Debye *et al.*, 1957; Mätzler, 2002]. As a result, measurements exist of snow microstructure as a visual grain size, specific surface area, optical grain radius, or correlation length. Not all of these measurements are easy to obtain and not all microwave emission models can use each measurement directly. The optimal choice of measurement results from appropriate trade-offs between resolution and practicality, allowing a sensible match between scales of measurement and simulation.

As variability in snow properties is so difficult to capture at the satellite scale, it seems reasonable to look at the much smaller scale of suborbital or ground-based sensors to test microwave models, where the potential exists to characterize snow properties more thoroughly. The use of ground-based passive microwave measurements to evaluate forward radiative transfer models, which use in situ snowpack properties, has been undertaken before [Brogioni *et al.*, 2009; Durand *et al.*, 2008; Kim and England, 2003; Mätzler and Wiesmann, 1999; Montpetit *et al.*, 2013; Rees *et al.*, 2010; Roy *et al.*, 2013; Tedesco *et al.*, 2005]. However, measured snowpack properties are commonly limited to a single vertical profile, often in snow pits excavated outside of the sensor footprint because of the need to maintain a consistently undisturbed measurement area. Ideally, for thorough evaluation, measurements of snowpack properties should be made throughout the horizontal extent of sensor footprints, and at a vertical resolution which at least matches the scale at which the snowpack properties interact with the passive microwave radiation (19 and 37 GHz approximately equate to wavelengths of 15 and 8 mm). Consequently, the aim of this study is to understand the impact of subfootprint spatial variability in snowpack properties on measured and simulated brightness temperatures at the plot scale. Resulting objectives are the following to: (1) present a new methodological framework that allows centimeter-scale simulations of brightness temperatures from two-dimensional (2-D) measurements of snowpack properties within footprints of ground-based passive microwave radiometers, (2) evaluate the

minimization of simulation bias with grain scaling factors and three different emission model extinction coefficients in relation to measurement of snowpack properties, (3) identify sensitivity of simulated brightness temperatures to the following: (i) uncertainties in field measurements, (ii) translation of 1-D profiles to 2-D stratigraphy, and (iii) experimental amalgamation of stratigraphic layering.

2. Methods

Measurements of snowpack properties were made at a sub-Arctic site (58.73°N, 93.82°W) near Churchill, Manitoba, Canada, as part of an experiment on the emission and backscattering properties of seasonal snow cover [Derksen *et al.*, 2012]. Measured brightness temperatures from ground-based microwave radiometers were compared with brightness temperatures from a multilayer snow emission model, which was initialized with high horizontal and vertical resolution measurements of snowpack properties across an approximately 4.5 m trench. The field measurements taken, the methods to translate snow properties across the trench, and the simulations of the microwave brightness temperature are all described in the following sections.

2.1. Field Measurements

Passive microwave radiometers at 19 and 37 GHz (dual polarized) were mounted side-by-side on a moveable sled, approximately 1.55 m above the snow surface at an incidence angle of 53°. The radiometer design has a 3 dB half-power beamwidth of 6°. The ground footprints of the sled-mounted radiometers were elliptical with a far width of 0.29 m and a depth of 0.45 m. Uncertainty in measured brightness temperatures was < 2 K at each frequency and polarization, based on sequential calibrations using cold (liquid nitrogen) and warm (microwave-absorbing material) targets [Derksen *et al.*, 2012].

On 12 April 2010 brightness temperature measurements (five at 19 GHz, four at 37 GHz) were made at nine positions along a linear transect so that the overlapping footprints covered a 3.8 m horizontal extent. At each position, brightness temperatures were averaged from between 200 and 400 individual measurements with a 1 s integration time. The standard deviation at each measurement position and each frequency was < 0.3 K. Five vertical profiles of snow temperatures were recorded within the radiometer footprints along the transect; each profile measured temperatures at the snow-ground interface and at 4 cm increments upward through the snowpack. In addition, brightness temperature measurements were made at this site on nine occasions throughout the winter, beginning 25 November 2009, which provided a seasonal context to the measurements on 12 April 2012.

Directly after radiometer measurements were made on 12 April, a 4.5 m trench was excavated through the center points of the radiometer footprints. Following protocols in Tape *et al.* [2010], the trench face was prepared for near-infrared (NIR) photographs (850 nm center wavelength) to be taken along its length. A centimeter-scale Crain measuring staff was positioned horizontally above the trench to allow georeferencing of NIR imagery along the trench face.

At three positions (75, 185, and 355 cm) along the trench, vertical profiles of snowpack stratigraphy, density and specific surface area per mass of ice (SSA_m) were measured. Density measurements, using a 183 cm³ triangular cutter (3 cm high), were made within coherent stratigraphic layers that were identified in the field. Measurements of specific surface area (SSA_m) were made using a 1310 nm laser mounted with an integrating sphere [Montpetit *et al.*, 2012]. Snow samples for SSA_m measurements were taken using a 226 cm³ cylindrical cutter (4 cm diameter) inserted vertically through the snowpack. Between five and seven samples at successively increasing depths were made per vertical profile, typically one per snow layer within the profile. The effective diameter (d_{eff}) of the sample grain size [Grenfell and Warren, 1999] was determined from the SSA_m following Gallet *et al.* [2009] and Montpetit *et al.* [2012]:

$$d_{\text{eff}} = \frac{6}{\rho_i \cdot SSA_m} \quad (1)$$

where ρ_i is the density of ice (916 kg m⁻³ for SSA_m given in m² kg⁻¹).

NIR images of adjacent sections of the trench were visually stitched together using positions along the measuring staff as control points. A single-stitched image of the entire trench was then visually examined and layer boundaries were identified at a 1 cm horizontal resolution (Figure 1). A leveled string, suspended horizontally above the trench and visible in all images, allowed the positions of snowpack layer boundaries to

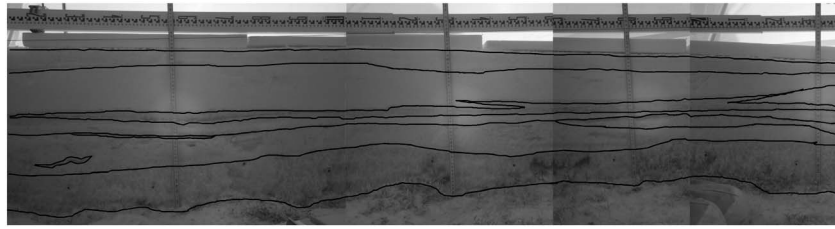


Figure 1. Example of layer boundary identification (black lines) on a 2.5 m section of the stitched trench image.

be adjusted with reference to a level surface. Consequently, a georectified 2-D array of internal snowpack layering was produced allowing discrete layers to be identified along the trench (Figure 2). As a guide for others, the time taken for the entire field procedure (radiometer measurements, trench excavation, and snow property characterization) was approximately 3 h.

2.2. Translating 1-D Profile Measurements to 2-D Stratigraphy

A complete 2-D array of snowpack properties (density, grain size, and temperature) was created from one-dimensional (1-D) profiles. Relating the measurements of snowpack properties from vertical profiles measured in the field, to stratigraphy derived from NIR images, was not straightforward. First, layers identified in the field from visual identification and hardness testing (herein collectively termed “manual inspection”) did not necessarily match layers that were identified from NIR photos. Second, as temperatures were point measurements at spacing of 4 cm in the vertical, and SSA and density measurements corresponded to layers identifiable in the field, not all layers identified from NIR images coincided with measurements. Consequently, some subjectivity was introduced by translating snowpack measurements from layers identified by manual inspection to layers identified using NIR.

Manual inspection of the snowpack was carried out at three locations along the trench: at 75 cm, 185 cm, and 355 cm. To translate the snow properties across the trench, the NIR-derived stratigraphy was extracted at these locations. Densities of layers 1 to 9 and 12 were taken directly from the measurements, as shown in Figure 3a. Effective grain sizes for these layers were also taken directly from measurements, as shown in Figure 3b. Where more than one measurement was available for a particular layer, the mean of the measurements was used.

As layer 10 was not present in the three manually inspected profiles, estimates of the density and grain size were obtained by averaging the respective properties of layers 5, 8, and 9, of which layer 10 was assumed to be a continuation. As layer 11 was also not present in manual profiles, the density and grain size was assumed

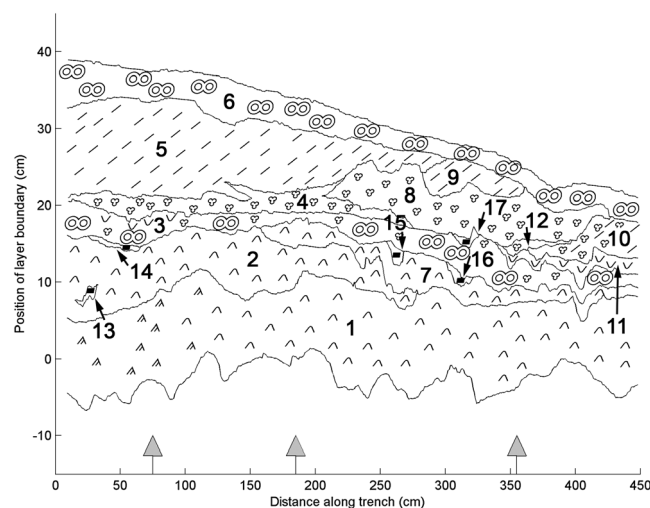


Figure 2. Snowpack layering (shaded and numbered) from NIR imagery, upward arrows (grey-filled arrowheads) indicate locations of manual profiles. Symbols describe snow type following the classification of Fierz *et al.* [2009]. Numbering relates layers to measurements in Table 1.

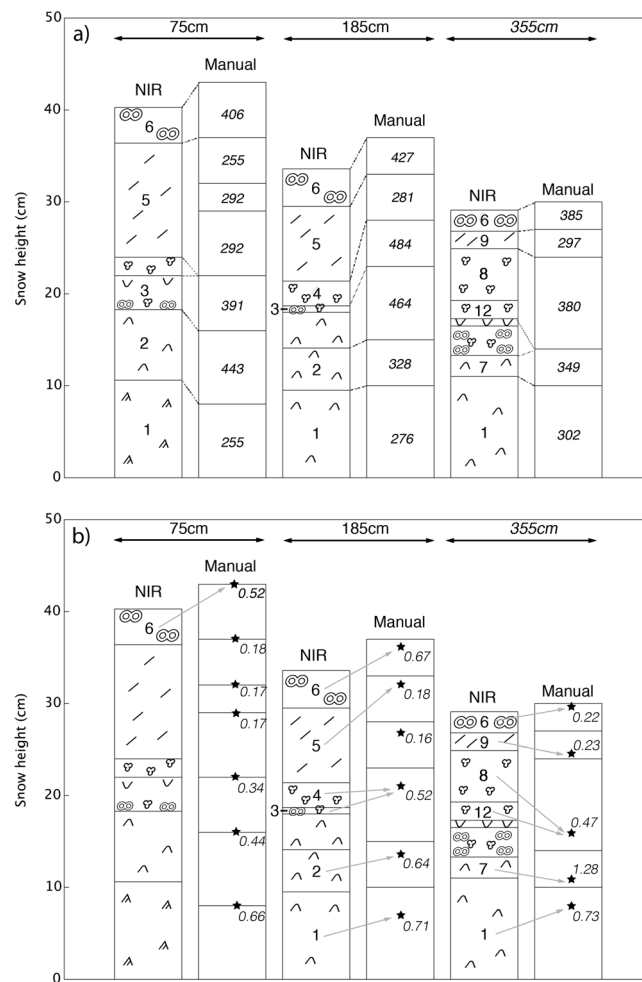


Figure 3. (a) Translating densities (in kg m⁻³) from manual vertical profiles to NIR layers, (b) translating effective grain diameters (in millimeters) from manual vertical profiles to NIR layers, and stars represent the location of measurements within the profiles. Symbols describe snow type following the classification of Fierz et al. [2009].

to be the same as for layer 7 due to the similarity of their appearances in NIR images. Layers 13 to 17 were classified as ice lenses from NIR images and are treated as such in the microwave emission model.

In order to derive unique physical temperatures for each layer, a mean temperature profile was first derived from the five vertical profile measurements. Secondly, a histogram of layer heights was calculated from the NIR stratigraphy and the mean height occupied by each layer was determined. The temperature of each layer was assumed to be the temperature at the same height from the mean observed temperature profile. The soil temperature was derived from an average of the five basal temperatures and was found to be -2.9°C with a standard deviation of 0.1°C .

2.3. Snow Emission Model Experiments

As a result of translating measured densities (ice lenses were assumed a constant density of 916 kg m^{-3}), grain sizes (d_{eff} derived from the SSA) and temperatures throughout the trench, each NIR layer had a single value describing each of the three snowpack properties (Table 1). These properties were applied to the 2-D array of snowpack layering and joined to a single subnivean layer describing the soil properties at the ground-snow interface. The soil was considered as a homogeneous, quasi-infinite layer with constant values of roughness, permittivity, and temperature across the trench. The mean of the temperature measurements at the soil-snow interface was used for the soil temperature. Soil roughness was calculated from the root mean square of the snow-soil interface height, relative to a 50 cm running mean (considered to be the footprint of the radiometer), and was calculated to be 10.77 mm. The permittivity of the frozen soil was

Table 1. Snowpack Layer Properties Throughout the Trench^a

Layer	Density (kg m ⁻³)	Effective Grain Diameter (mm)	Temperature (°C)
1	278	0.72	-3.0
2	386	0.64	-3.4
3	391	0.52	-3.6
4	484	0.52	-4.0
5	280	0.18	-4.8
6	406	0.47	-5.0
7	349	1.28	-3.4
8	380	0.47	-4.1
9	297	0.23	-4.5
10	319	0.30	-3.6
11	349	1.28	-3.4
12	380	0.47	-3.5
13	916	NA	-3.4
14	916	NA	-3.7
15	916	NA	-3.5
16	916	NA	-3.3
17	916	NA	-3.6
Mean	358 ^b	0.59	-3.8
Min	278 ^b	0.18	-5.0
Max	484 ^b	1.28	-3.0

^aNA, not applicable.

^bThis denotes excluding ice lens densities.

assumed to be 6-j, according to previous work [Pulliainen *et al.*, 1999] and based on measurements taken by Hallikainen *et al.* [1985].

Vertical profiles of snow and soil information were then extracted from this array at each centimeter along the trench as inputs to the multilayer Helsinki University of Technology (HUT) snow emission model [Lemmetyinen *et al.*, 2010]. The HUT model is a semiempirical radiative transfer model that uses parameters describing snowpack properties, such as density, grain size, and temperature, to estimate both scattering and absorption of microwave energy. The definition of total extinction of microwave energy in snow is based on an empirical relation, obtained using measurements of snow samples in laboratory conditions, representing a range of naturally

formed snow in southern Finland; Hallikainen *et al.* [1987] give a relationship between the extinction of microwaves in snow, frequency (ranging between 18 and 60 GHz) and particle diameter (<1.6 mm) so that

$$\kappa_e = 0.0018f^{2.8}d^{2.0} \quad (2)$$

where κ_e is the extinction coefficient (dB/m), f is the frequency (GHz), and d is the snow grain diameter (mm). Here it is important to note that d in the snow slab samples, used to derive equation (2), were quantified following the technique defined by Fierz *et al.* [2009]. Therefore, the compatibility of the HUT model to any other measures of snow microstructure, including optical-equivalent grain size, requires scaling of the measure to d . Mätzler [2002] notes that the optical-equivalent grain size is typically smaller than d , with the exception of perfectly round grains not present in nature.

Kontu and Pulliainen [2010] reported a similar formulation

$$\kappa_e = 0.08f^{1.75}d^{1.8} \quad (3)$$

which was optimized for deeper and denser snow with larger grain sizes than taiga snow. In the experimental data used by Hallikainen *et al.* [1987], the maximum diameter of snow grains was 1.6 mm thus giving an approximate range of validity for equation (2). To account for overestimation of extinction in the presence of large grains, Roy *et al.* [2004] proposed an alternate formulation using two empirically determined constants to account for multiple scattering by densely packed ice particles. Following Roy *et al.* [2004]

$$\kappa_e = \gamma(f^4 d^6)^\delta \quad (4)$$

where γ and δ are 2 ± 1 and 0.20 ± 0.04 , respectively. Roy *et al.* [2004] applied a model inversion scheme to derive γ and δ from model simulations compared with airborne observations. The observed (and measured) snow conditions thus represent average conditions over a natural snowpack, whereas Hallikainen *et al.* [1987] measured slab samples of relatively homogeneous snow. The formulation by Roy *et al.* [2004] thus includes effects inherent to natural snow such as layering. For clarity in interpretation of HUT model outputs, an optional component of HUT [Kontu and Pulliainen, 2010] that converted grain diameter from manual inspection (d_{obs}) to an effective microwave grain size (d_{eff})

$$d_{\text{eff}} = 1.5 \cdot (1 - e^{-1.5 \cdot d_{\text{obs}}}) \quad (5)$$

Table 2. Summary of Model Sensitivity Experiments

Experiment Purpose	Experiment Name	Experimental Method	Random Variation Applied
Testing measurement uncertainty	Density	Change measured densities	$\pm 50 \text{ kg m}^{-3}$ in each snow layer
	Grain size	Change measured grain sizes	$\pm 10\%$ in each snow layer
	Layer boundary	Change layer boundary positions	$\pm 1 \text{ cm}$ to each boundary point
	Ice lens identification	Extend, add, or exclude ice lenses	Up to six ice lens extensions (thickness 0.1–0.5 mm)
Testing translation uncertainty (1-D to 2-D)	Unmeasured layers	Apply density and grain sizes measured throughout trench to unmeasured layers	Density for each layer between 278 and 484 kg m^{-3} . Grain diameter for each layer between 0.18 and 1.28 mm
	Ice lens or crusts	Simulate crusts where ice lenses were originally identified	Crust density between 500 and 916 kg m^{-3}

was not used in this study because SSA was measured rather than estimating grain size from crystal card analysis. Consequently, any relation between the model parameter and SSA-derived grain diameter is likely to be different to the relation between the model parameter and crystal card grain diameter (equation (5)).

Twelve brightness temperatures were simulated at each horizontal position, dependent on frequency (19 or 37 GHz), polarization (horizontal or vertical), and specified extinction coefficient model. The resulting spatial variability across the trench of simulated brightness temperatures and bias between measured and simulated brightness temperatures were calculated. Scaling factors, from 1.5 to 6.0 in increments of 0.1 as per *Langlois et al.* [2012], were applied to grain sizes of all layers in order to minimize the bias between measured and simulated brightness temperatures. Then, subsequent to this optimization, sensitivity experiments (Table 2) were performed to test the impact on simulated brightness temperatures of uncertainties in field measurements and translation of physical properties from 1-D profiles to 2-D layers.

Ensembles of 100 simulations of brightness temperatures across the trench were generated at each configuration of frequency, polarization, and extinction coefficient for all sensitivity experiments. Mean values of the ensembles were then compared to different frequencies and polarizations of measured brightness temperatures. A random measurement error was applied in turn to layer densities (up to $\pm 50 \text{ kg m}^{-3}$), effective grain diameters (up to $\pm 10\%$), or layer boundary heights (up to $\pm 1 \text{ cm}$) in each of the ensembles.

To test uncertainties in ice lens identification, the NIR stratigraphy was reexamined and the maximum potential ice lens extent was identified, compared to ice extents identified through manual inspection. As a result, six possible extensions to ice lenses in Figure 2 were identified from the NIR image: (1) Layer 14 (on top of layer 2) extended between 0.25 and 0.8 m, (2) layer 15 (on top of layer 7) extended between 1.6 m and original position, (3) additional ice lens (on top of layer 3) between 2.0 and 2.85 m, (4) additional ice lens (on top of layer 7) between 2.75 and 2.85 m, (5) layer 17 (on top of layers 3 and 11) extended between 3.05 and 4.5 m, and (6) layer 16 (on top of layer 7) extended between 3.05 and 4.5 m.

Each of the six possible ice lens additions were randomly applied or excluded in each of the 100 trench simulations, so an individual simulation may have no extensions, all extensions, or a few extensions applied. A single thickness of between 0.1 and 0.5 cm was randomly applied to each extended or additional lens.

To test the impact of deriving snow properties for layers that were not measured directly, random densities and grain sizes between the field-measured maximum and minimum throughout the trench were applied to layers 3, 4, 7, 8, 10, 11, and 12, in each of the 100 simulations. In the last sensitivity experiment, to simulate layers 13–17 as snow crusts rather than ice lenses, a single density between 500 and 916 kg m^{-3} was randomly assigned to all crusts in each of the 100 simulations. As these layers were treated as high-density snow layers rather than ice, a snow grain size was required, which was assumed to be the same as the layer adjacent or surrounding the ice crust.

Finally, to test the impact of layer amalgamation on optimized simulated brightness temperatures, vertical profiles of snowpack layering were represented in four different configurations (Figure 4) of increasing complexity: (1) one layer, vertically weighted integration of all layers; (2) two layers, top layer contained layer 6; bottom layer comprised the rest of snowpack; (3) three layers, top layer contained layer 6; middle layer comprised layers 3, 4, 5, 8, 9, 10, 11, 12, and 17; bottom layer comprised layers 1, 2, 7, 13, 14, 15, and 16; and (4) n layer, original stratigraphy.

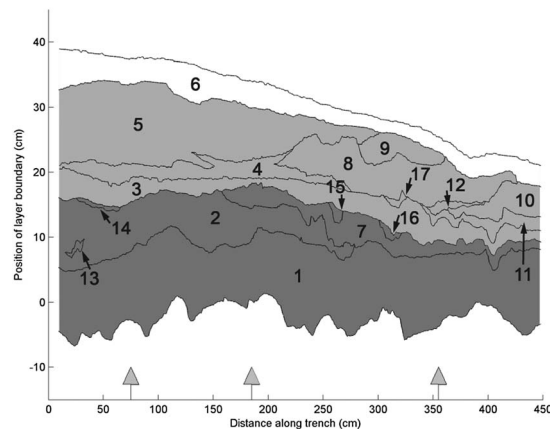


Figure 4. Visualization of the representation of snowpack stratigraphy in the layer amalgamation experiment. One layer: white and grey areas all combined into one layer; Two layers: white is upper layer, grey combined is lower layer; Three layers: white is upper layer, light grey is middle layer, dark grey is lower layer; n layer: individual layers denoted by black boundary lines.

the length of the trench. Layers were more often discontinuous than continuous even over the short trench distance.

Variability of the base layer thickness, consisting of depth hoar (layer 1 in Figure 2), was heavily influenced by the undulating hummocky ground surface layer, while the much less variable surface layer (layer 6) thickness was a function of the compaction and redistribution of recent snowfall by wind. However, between these two layers, the shape, thickness, and extent of internal layers were relict features of past meteorological events (including wind redistribution) and metamorphic activity (both kinetic grain growth and melt/refreeze). For example, layer 4, which was the densest layer consisting of an amalgam of wind-packed snow, numerous fine crusts, and very large grains trapped between the series of crusts. Between 130 and 224 cm, this layer had a distinct anvil shape most likely the result of a relict surface crust that was excavated along lines of structural weakness by wind scour and in-filled by a subsequent snowfall event. Variability of other internal discontinuous layers resulted from localized hardening of the surface layer (e.g.,

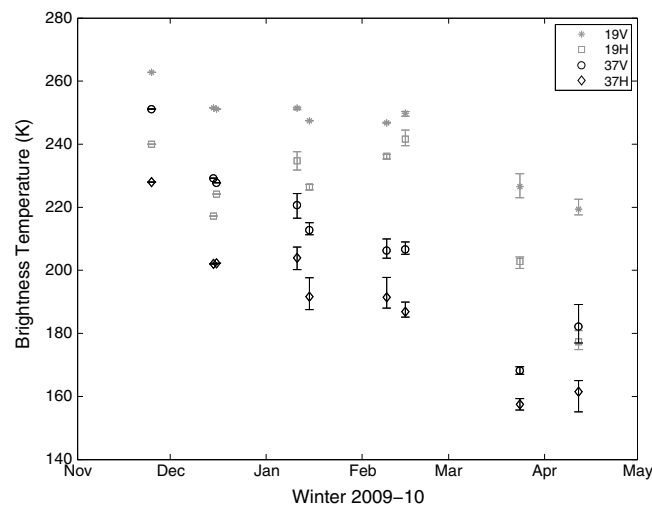


Figure 5. Seasonal decline in mean measured brightness temperatures at the trench site. Error bars indicate range of brightness temperatures: measurements were made at one location along the trench in November and December, at three locations in January to March, and at five locations in April.

In each layer configuration: (1) the total thickness and SWE of the vertical profiles were kept constant at each position along the trench; consequently, density was allowed to vary by horizontal position, (2) grain size was calculated as a thickness-weighted average of snow layers, and (3) temperature was calculated as a thickness-weighted average of snow and ice layers.

3. Results

3.1. Two-Dimensional Snowpack Properties

Snowpack stratigraphy across the 450 cm trench was complex (Figure 2). The number of layers in any single vertical profile ranged between six and eight, and out of 17 horizontally identifiable layers only three were continuous throughout

sun crusts and wind packing) providing resistance to wind erosion. The spatial incoherence of this resistance and the relative susceptibility of the layer beneath the surface, in part a function of metamorphism, caused the discontinuous layering pattern evident in Figure 2. Ice lenses within the trench resulted from recent surface melt percolating through the snowpack and collecting and refreezing at impermeable layer boundaries. Consequently, irregularly spaced ice lenses, which were relatively short in extent, increased the horizontal variability of snowpack properties. As a result, snow layer density and effective grain size ranged considerably (range of 206 kg m^{-3} and 1.10 mm ,

Table 3. Bias Between Mean HUT and Mean Measured Brightness Temperatures (K), Positive Values Indicate Simulations Overestimate Measured Brightness Temperatures, Range of Bias Across Extinction Coefficients in Parentheses

	Bias Before Grain Scaling Factors	Bias After Grain Scaling Factors
19H	51 (7)	0.2 (1.1)
19V	36 (8)	0.6 (0.3)
37H	64 (2)	−0.4 (3.5)
37V	68 (2)	−0.5 (2.2)

respectively), although physical temperatures were more conservative, with a range of 2.0°C around a mean of −3.8°C (Table 1).

3.2. Bias and Optimization of Simulated Brightness Temperatures

Repeated measurements of brightness temperatures at the trench site throughout the winter showed a seasonal decline (Figure 5), which accelerated after February as a result of increased snow crystal size and slight increases in mass. Brightness temperatures at this site were similar to measurements at surrounding forest, and open fen sites [Derksen *et al.*, 2012] suggesting they were typical of a broad range of sub-Arctic snowpack types. Simulated brightness temperatures, using original stratigraphy and measured SSA-derived grain diameters, were greater than measurements at all positions along the trench. Resulting mean biases of 36 to 68 K, depending on frequency and polarization (Table 3), were in part due to the low measured brightness temperatures in April. These mean biases were at least 13 K smaller at 19 GHz than 37 GHz, although the range in mean biases depending on the extinction coefficient used were larger at the lower frequency. As measurements of soil type and moisture were not taken, we could not completely discount the soil as a source of bias in simulated brightness temperature. However, soil surface temperatures were measured and were shown to be frozen (−2.9°C). Zhang *et al.* [2003] showed that soil type was of little importance for frozen soil and that the permittivity should be approximately 6-j, as applied in this study. Although it was possible that unfrozen soil beneath the frozen surface layer had an effect, the moisture-sensing depth of microwave radiation ranges from ~0.1 to 1 wavelengths [Marshall *et al.*, 2008]. Consequently, for wavelengths between 0.8 mm to 1.6 cm used in this study, it was unlikely that parameterization of the soil was the main cause of the difference between measured and simulated brightness temperatures.

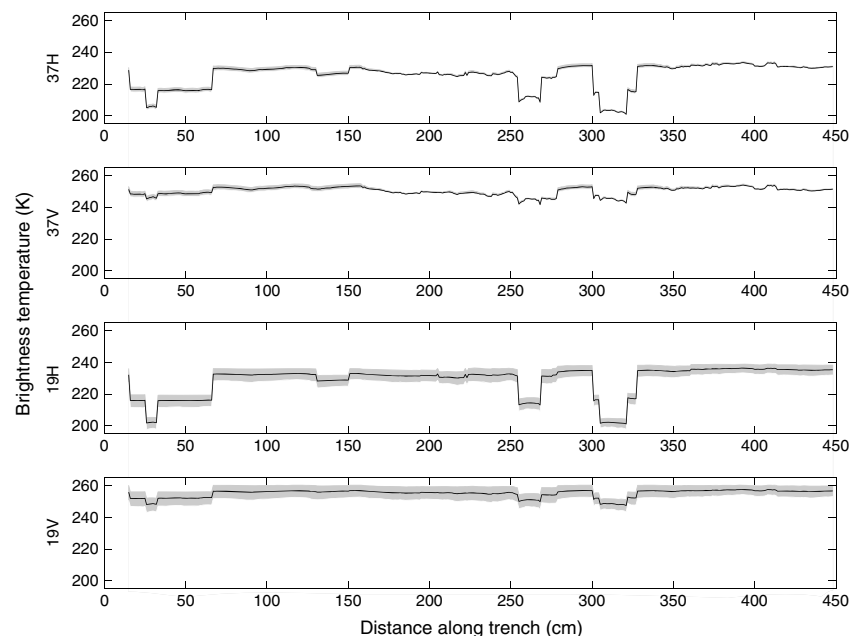
**Figure 6.** HUT brightness temperature simulations, before application of grain scaling factors, using all extinction coefficients models (mean = black line; range = shaded grey area).

Table 4. Optimal Simulated Grain Scaling Factor to Relate the Mean Simulated and Measured Brightness Temperatures for Each Combination of Frequency, Polarization, and Extinction Coefficient

Frequency/polarization	Extinction Coefficient		
	<i>Hallikainen et al.</i> [1987]	<i>Roy et al.</i> [2004]	<i>Kontu and Pulliainen</i> [2010]
19 V	4.2	3.3	3.2
19 H	5.3	4.9	4.2
37 V	2.6	4.4	2.8
37 H	2.7	4.6	2.8

The changes in simulated brightness temperatures throughout the trench were rapid and stepped rather than slow and incremental (Figure 6). At all these frequency-polarization combinations, step changes were greater in magnitude than the small spread in simulated brightness temperatures caused by the three different extinction coefficients, which varied only slightly within individual frequency-polarization combinations throughout the trench (Figure 6). The positions of the step changes were coincident with the positions of ice lenses, which showed a greater decrease in brightness temperatures (reducing bias by bringing simulated brightness temperatures closer to measured values) at H-pol than V-pol irrespective of frequency. Where a second ice lens appeared above another along the trench, a second step change occurred in the simulated brightness temperatures, leading to a greater drop in brightness temperature than for one ice lens alone.

Application of scaling factors to measured or simulated grain size, in order to improve simulated estimates of brightness temperatures, is becoming increasingly common [Langlois *et al.*, 2012; Montpetit *et al.*, 2013; Roy *et al.*, 2013]. In the current study, the optimal grain scaling factor was the scaling factor (to the nearest 0.1) which produced the best agreement between the mean measurements and the mean simulations for each combination of frequency, polarization, and extinction coefficient. Grain scaling factors varied between 2.6 and 5.3 (Table 4). At 19 GHz, the scaling factors for all extinction coefficients were greater at H-pol than V-pol, with the *Hallikainen et al.* [1987] coefficient requiring the largest optimal scaling factors at both polarizations. Conversely, at 37 GHz, there was little difference in scaling factors between polarizations, with the coefficient of *Roy et al.* [2004] requiring the largest optimal scaling factor. The resulting biases between mean measured and mean optimized brightness temperatures (Table 3) were very low (<0.6 K), with an increased range in biases across the three extinction coefficients at 37 GHz than at 19 GHz. Mean simulated brightness temperatures after application of scaling factors (Figure 7) showed greater variability along the trench than simulations without scaling factors

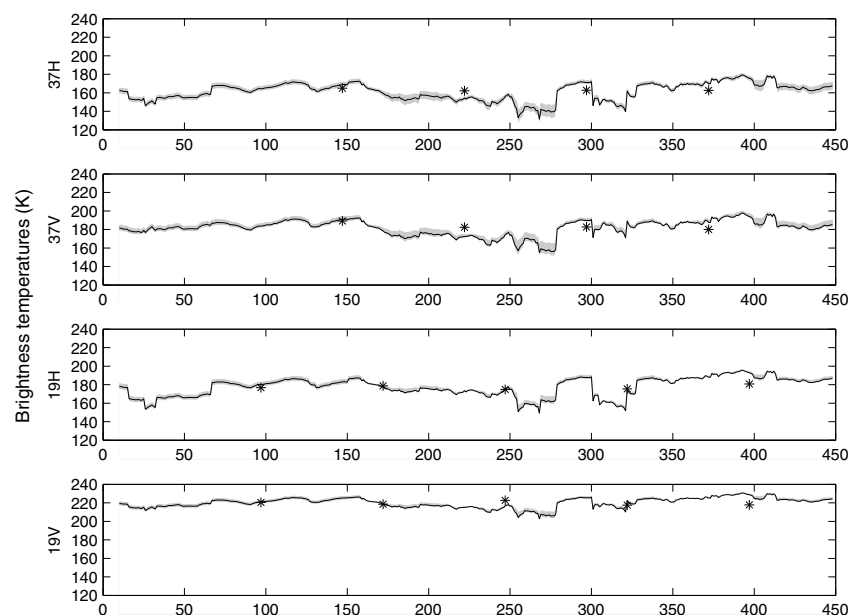


Figure 7. HUT brightness temperature simulations, after application of grain scaling factors, using all extinction coefficients models (mean = black line; range = shaded grey area) and measured brightness temperatures (asterisks).

Table 5. Bias of Simulated and Measured Brightness Temperatures (K) Throughout the Trench for Each Modeling Experiment

Experiment	Bias (Mean HUT After Grain Scaling Factors – Mean Measured)			
	19 V	19H	37 V	37H
Density	–0.3	–1.5	–1.9	–2.1
Grain size	0.3	–0.2	–1.1	–0.9
Layer boundary	2.5	3.5	2.8	3.4
Ice lens identification	–1.1	–6.6	–1.5	–5.5
Unmeasured layers	–3.2	–4.5	–7.5	–6.8
Ice lens or crusts	0.5	1.1	–1.3	–0.2

(Figure 6) because less radiation is transmitted through the snowpack. In addition, decreases in brightness temperatures coincident with the position of ice lenses were still evident but were less well defined than before application of scaling factors, and the range of the three extinction coefficients was lower throughout the 19 GHz simulations and greater in sections of 37 GHz simulations than before grain scaling factors were applied.

3.3. Model Sensitivity and Stratigraphic Representations

Bias as a result of model sensitivity experiments ranged between 3.5 and –7.5 K (Table 5). Application of snow properties to unmeasured layers produced biases across all combinations of frequency and polarization (–3.2 to –7.5 K), which were larger at H-pol than V-pol. The identification and extension of ice lenses also increased bias at H-pol (–5.5 to –6.6 K), but not at V-pol (–1.1 to –1.5 K). Identification of layer boundary positions was the only sensitivity experiment to consistently produce positive biases (simulation overestimation) between 2.5 and 3.5 K. The remaining experiments applying measurement uncertainty to densities and grain size, as well as simulation of ice lenses as crusts, had low biases all within 2.1 K of mean measured brightness temperatures.

Bias resulting from layer representation experiments ranged between –0.5 and 14.6 K (Table 6). The bias of the one-layer stratigraphic representation of the snowpack was the largest across all combinations of frequency and polarization (4.9–14.6 K); biases decreased as stratigraphic layer representations became increasingly realistic, except for changes at V-pol from one- to two-layer representations where there was no decrease in bias or change was negligible (0.2 K). For stratigraphic representations of one to three layers, biases at H-pol were always greater than V-pol at both frequencies and biases at 19 GHz were always greater than at 37 GHz for respective polarizations.

4. Discussion

4.1. Stratigraphic Variability

Wintertime hydrometeorological processes controlling snow deposition, redistribution, scour, temperature gradient metamorphism, and melt-refreeze produced an April snowpack in Churchill which had high two-dimensional stratigraphic variability (a maximum of eight layers in any one-dimensional profile). Such stratigraphic variability is characteristic of sub-Arctic snowpacks that cover vast areas of nonboreal land in the Northern Hemisphere around the timing of peak seasonal SWE; *Derksen et al.* [2009] showed that vertical profiles at 45 locations across a 2000 km transect had an average of six layers (and as many as nine), while *Sturm and Benson* [2004] showed similar complexity, in two dimensions, in Arctic snowpacks. Consequently, it is vitally important that this stratigraphic reality is adequately represented in 1-D by multilayer emission models, and measured brightness temperatures (integrated throughout three-dimensional (3-D) volumes of snow) are evaluated using distributions of simulated brightness temperatures within sensor footprints. The

Table 6. Bias of Simulated and Measured Brightness Temperatures (K) Throughout the Trench for Four Different Representations of Stratigraphic Layering

Layer Representation	Bias (Mean HUT After Grain Scaling Factors – Mean Measured)			
	19 V	19H	37 V	37H
One layer	5.8	14.6	4.9	11.5
Two layers	5.6	10.9	4.9	8.4
Three layers	3.4	8.0	2.5	6.0
<i>n</i> layer	0.6	0.2	–0.5	–0.4

new methodological framework presented here, which assigned measured physical snow properties (density, effective grain size, and temperature) to stratigraphic layering identified using NIR photos [Tape *et al.*, 2010] in a multilayer snow emission model (HUT), has enabled this for the first time.

Conceptually, 3-D measurements of snow properties would be ideal inputs to emission models, particularly as our theoretical understanding of 3-D multiple scattering of microwaves by densely packed ice grains improves [Tsang *et al.*, 2013]. However, our current ability to accurately measure 3-D variability in snow microstructure, e.g., X-ray tomography [Heggli *et al.*, 2011], over spatial extents large enough to adequately resolve variability within the footprints of remote-sensing instruments (even of ground-based sensors) is not yet practical. Consequently, measurement of 2-D variability in this manner provides an appropriate trade-off between measurement resolution and practicality, capturing horizontal variability in the vertical gradients of grain size and density that result from the meteorological and metamorphic processes which control snowpack microstructure.

4.2. Bias and Scaling Factors

The horizontal variability across the trench of measured brightness temperatures in any particular combination of frequency and polarization was low (Figure 7). Across the trench, from left to right, the increase in mean grain size of vertical profiles (0.48 to 0.66 mm from linear trendline analysis) and the increased number of layer boundaries will cause increased scattering. Increased scattering will partially compensate for the decrease in SWE from left to right across the trench. In addition, reduced horizontal variability of measured brightness temperatures may be caused by the following: (1) averaging of the integrated signal received at the antenna from overlapping measurements of the main beam between adjacent radiometer footprints, (2) approximately 50% of the power integrated by the radiometer antenna coming from outside the 3 dB field of view, and (3) possible 3-D attenuation of the variability in snowpack properties exhibited by 2-D slices across footprints (e.g., discontinuous ice lenses). Simulated brightness temperatures were higher in magnitude than measurements, with a larger horizontal variability mainly influenced by the location of ice lenses. The resulting large biases required application of scaling factors to grain size in order to provide a better fit between simulated and measured brightness temperatures, thereby compensating for the uncertainty relating optical SSA to microwave model grain size input. Previous studies have applied scaling factors to optical grain size radius in DMRT-ML [Brucker *et al.*, 2011], to correlation length derived from simulated grain size in Microwave Emission Model of Layered Snowpacks (MEMLS) [Langlois *et al.*, 2012], and to correlation length from SSA in MEMLS [Montpetit *et al.*, 2013]. Scaling factors of between 0.1 and 2.85 have resulted. Only Roy *et al.* [2013] has previously attempted this for HUT, using SSA measurements of grain size. Using an optimal grain scaling factor of 3.7, Roy *et al.* [2013] concluded optical measurement of SSA will underestimate the maximum diameter from manual inspection (D_{\max}) as the relationship between SSA and D_{\max} is nonlinear [Langlois *et al.*, 2010]. In the current study we extend previous work, quantifying the impact of three empirical formulations for the snow extinction coefficient. Although the mean of all scaling factors across combinations of frequency, polarization and extinction coefficient is similar (3.8) to that reported by Roy *et al.* [2013], the spread of optimal scaling factors for individual combinations, 2.6 to 5.3 (Table 4), quantifies relative differences in the ability of extinction coefficient formulations to compensate for the underestimation of extinction properties by the HUT model.

Grain scaling factors tentatively link an effective grain size derived from optical measurements to an effective grain size required for scattering and emission at microwave frequencies. Grain scaling factors reported in this study would equate to layers with effective grain diameters of between 0.5 and 6.8 mm, requiring consideration of microstructure beyond the size of individual grains [Löwe *et al.*, 2011], such as conglomerates. In addition to scatter and emission by grains, the increased sensitivity of H-pol to ice lenses, previously reported in HUT [Rees *et al.*, 2010] and MEMLS [Durand *et al.*, 2008; Montpetit *et al.*, 2013], could be a factor causing the larger scaling factors in H-pol than V-pol at both frequencies, especially at 19 GHz. Ice lenses, which were discontinuous throughout the trench, cause greater scatter at H-pol than is estimated by the HUT model, indicating that scaling factors at individual polarizations reflect more than just volume scattering by grains within layers.

The variability of extinction coefficients with frequency is strongly grain size dependent; Figure 8 helps to explain differences between optimal scaling factors for different extinction coefficients (Table 4). When grain size is small, there is little difference between the impact of the different coefficients, independent of frequency. However, as grain size increases, at 19 GHz, the extinction coefficients of Roy *et al.* [2004] are

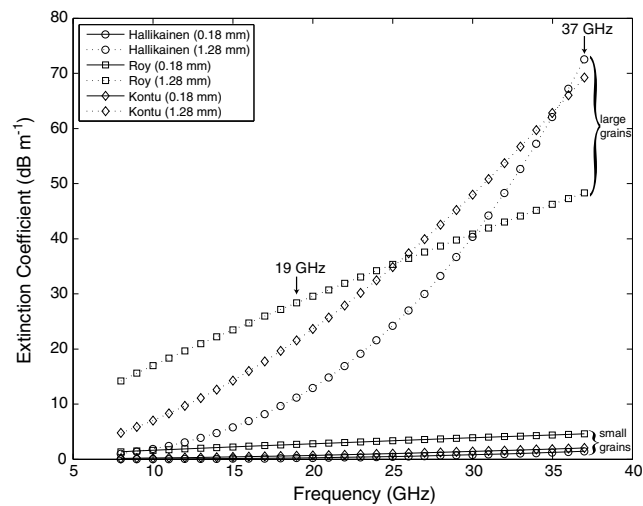


Figure 8. Extinction coefficients as a function of frequency at maximum and minimum measured effective grain diameters.

greater than *Kontu and Pulliainen* [2010], which are in turn greater than *Hallikainen et al.* [1987]. At 37 GHz, this order reverses. Scaling factors compensate for the differences in extinction coefficient values at each frequency, so that by using scaled grain sizes, the different extinction models equate to the same extinction coefficient. Table 4 shows *Hallikainen et al.* [1987] and *Kontu and Pulliainen* [2010] coefficients required lower compensation by scaling factors at 37 GHz than *Roy et al.* [2004], whereas at 19 GHz V-pol (excluding H-pol due to the previously discussed influence of ice lenses), the coefficients of *Kontu and Pulliainen* [2010] and *Roy et al.* [2004] required lower compensation than *Hallikainen et al.* [1987]. Used in this manner, the scaling factor has increasing physical basis as a proxy for the influence of large grains on scattering and absorption. As stratigraphic variability can be high in sub-Arctic snowpacks, due to hydrometeorological and metamorphic processes interacting with subnivean vegetation and ground roughness, it is important when modeling brightness temperatures to consider the proportions of large (hoar) and small (wind slab) grains in distributions of 1-D profiles rather than a single profile alone.

4.3. Sensitivity to Model Inputs and Layer Amalgamation

After experimentally adding measurement uncertainties to layer boundary positions, densities, and grain size, the impact of these uncertainties on simulated brightness temperatures was shown to be low (all within 3.5 K of mean measured brightness temperatures). This suggests that the level of error in field measurements of these variables and the framework for translating them into a snow emission model were sufficient for the purpose of model evaluation. The simulation of crusts where lenses were identified showed similar low levels of bias. However, rather than suggest that the distinction between lenses and crusts are unimportant for scattering, this may be a limitation of the simplicity in which the HUT model could be experimentally forced to replicate real crusts. Field observations revealed thin crusts resulting from insolation or wind hardening, with large grains adhering to the underside of the crusts (e.g., intermittently present throughout layer 4). The large grains most likely resulted from metamorphism where upward vapor transport was limited by impermeable crusts. Large gradients in dielectric properties and grain size, which were present between discontinuities in ice crusts and snow, have important scattering and reflective properties [Kim, 2006; Mätzler, 1996]. Such discontinuities were only partially accounted for by experimental changes in density as, for these simulations of crusts, grain size was made constant with that of adjoining layers. However, as the air content in ice lenses can decrease the density by more than half [Mätzler and Wiesmann, 1999] and density of ice lenses influences scattering potential [Durand et al., 2008], it is important that density of ice lenses and crusts are more accurately reflected by HUT and more reliable field measurements are obtained.

The importance of correctly identifying the spatial extent of discontinuous ice lenses at H-pol agreed with *Rees et al.* [2010] who showed the influence of continuous ice lenses was not adequately represented by the implementation of two-layer HUT. Simulated brightness temperatures were much less sensitive at V-pol.

Where measurements of grain sizes and densities in individual layers were not available, assigning layers random values within the range of measured values shown in Figure 3 only created a maximum absolute bias of 7.5 K. This test, of potentially the weakest part of the methodological framework, suggested that the methods translating 1-D profiles to 2-D stratigraphy were appropriate.

The biases associated with layer amalgamation have implications for the wider application of HUT over regional to global scales, for example, in data assimilation products such as GlobSnow, where realistic vertical complexity in snowpacks cannot be characterized from near-real-time snow observations at climate stations [Takala *et al.*, 2011]. The increase in bias from the original stratigraphy to a one-layer representation was more pronounced (more than double) at H-pol than V-pol at both frequencies, most likely highlighting sensitivity of H-pol to ice lenses and the necessity to include their scattering capability in large-scale applications. For the purpose of high resolution, distributed, physical snow modeling at the regional scale, a three-layer snowpack representation approaches current computational limitations, e.g., SNODAS [Rutter *et al.*, 2008]. Consequently, improvements in accuracy provided by a three-layer approach to emission modeling will be of interest to future assimilation schemes that combine physical and emission models. In this study, bias of the three-layer representation was between 51 and 58% of the bias at one-layer representation. To achieve a further decrease of a similar percentage magnitude would require the original stratigraphy.

5. Conclusions

Two-dimensional stratigraphic layering was highly variable (up to eight layers in any one-dimensional profile) throughout a 4.5 m trench in a snowpack at Churchill, Manitoba, Canada, in April 2010. The variability of stratigraphic layering in the trench was highly representative of sub-Arctic and Arctic snowpacks.

Large biases (36 to 68 K) between simulated and measured brightness temperatures were minimized (−0.5 to 0.6 K) by the application of scaling factors to grain size. Grain scaling factors (2.6 to 5.3) compensated for the uncertainty relating optical SSA to HUT model grain size inputs and quantified relative differences in the ability of extinction coefficients to compensate for underestimation of extinction and absorption properties by the HUT model. Such large grain scaling factors suggest that the HUT model requires consideration of microstructure beyond the size of individual grains (e.g., conglomerates) and accurate representation of ice lenses, particularly for simulations at horizontal polarizations.

The variability of extinction coefficients with frequency is strongly grain size dependent. When grain size was small, independent of frequency, there was little difference between the impact of the different extinction coefficients. However, with increasing grain size, differences between coefficients at different frequencies became increasingly variable.

Consequently, when modeling brightness temperatures, it is important to consider the proportions of large (hoar) and small (wind slab) grains in distributions of 1-D profiles rather than a single profile alone, especially in sub-Arctic snowpacks where stratigraphic variability can be high.

Experiments to assess model sensitivity to measurement uncertainty and uncertainty in translating 1-D profiles to 2-D stratigraphy suggested that the level of error in field measurements and the methodological framework used to apply them in a snow emission model were satisfactory. The importance of correctly identifying the spatial extent of discontinuous ice lenses at H-pol was also demonstrated. In the layer amalgamation experiment, this study showed that a three-layer representation of the snowpack reduced the bias (across combinations of frequency, polarization, and extinction coefficients) to between 51 and 58% of the bias in a one-layer representation.

References

- Barnett, T. P., J. C. Adam, and D. P. Lettenmaier (2005), Potential impact of a warming climate on water availability in snow-dominated regions, *Nature*, *438*, 303–309.
- Brogioni, M., G. Macelloni, E. Palchetti, S. Paloscia, P. Pampaloni, S. Pettinato, E. Santi, A. Cagnati, and A. Crepaz (2009), Monitoring snow characteristics with ground-based multifrequency microwave radiometry, *IEEE Trans. Geosci. Remote Sens.*, *47*(11), 3643–3655.
- Brown, R. D. (2000), Northern hemisphere snow cover variability and change, 1915–97, *J. Clim.*, *13*(13), 2339–2355.
- Brown, R. D., and R. O. Braaten (1998), Spatial and temporal variability of Canadian monthly snow depths, 1946–1995, *Atmosphere-Ocean*, *36*(1), 37–54.
- Brucker, L., G. Picard, L. Arnaud, J.-M. Barnola, M. Schneebeli, H. Brunjail, E. Lefebvre, and M. Fily (2011), Modeling time series of microwave brightness temperature at Dome C, Antarctica, using vertically resolved snow temperature and microstructure measurements, *J. Glaciol.*, *57*(201).

Acknowledgments

We would like to thank Bryn Hubbard, Martin Schneebeli, and four anonymous reviewers for their insightful and constructive comments that greatly improved this manuscript. Funding for the field measurements used in this study was provided by Environment Canada and the Canadian Space Agency. Logistical support in the field was provided by the Churchill Northern Studies Centre (thanks to LeeAnn Fishback, Carley Basler, and Clifford Paddock). Sandells acknowledges support from the Natural Environment Research Council (NERC) and the National Centre for Earth Observation (NCEO).

- Chang, A., J. Foster, and D. Hall (1987), NIMBUS-7 SMMR derived global snow cover parameters, *Ann. Glaciol.*, **9**, 39–44.
- Cline, D., K. Elder, and R. Bales (1998), Scale effects in a distributed snow water equivalence and snowmelt model for mountain basins, *Hydrol. Processes*, **12**, 1527–1536.
- Davenport, I. J., M. J. Sandells, and R. J. Gurney (2012), The effects of variation in snow properties on passive microwave snow mass estimation, *Remote Sens. Environ.*, **118**, 168–175.
- Debye, P., H. R. Anderson, and H. Brumberger (1957), Scattering by an inhomogeneous solid. II. The correlation function and its application, *J. Appl. Phys.*, **28**(679), 679–683.
- Derkson, C., A. Walker, and B. Goodison (2003), A comparison of 18 winter seasons of in situ and passive microwave-derived snow water equivalent estimates in Western Canada, *Remote Sens. Environ.*, **88**, 271–282.
- Derkson, C., A. E. Walker, B. E. Goodison, and J. W. Strapp (2005), Integrating in situ and multiscale passive microwave data for estimation of subgrid scale snow water equivalent distribution and variability, *IEEE Trans. Geosci. Remote Sens.*, **43**(5), 960–972.
- Derkson, C., A. Silis, M. Sturm, J. Holmgren, G. E. Liston, H. Huntington, and D. Solie (2009), Northwest Territories and Nunavut snow characteristics from a sub-Arctic traverse: Implications for passive microwave remote sensing, *J. Hydrometeorol.*, **10**(2), 448–463.
- Derkson, C., P. Toosea, J. Lemmetyinen, J. Pulliainen, A. Langlois, N. Rutter, and M. C. Fuller (2012), Evaluation of passive microwave brightness temperature simulations and snow water equivalent retrievals through a winter season, *Remote Sens. Environ.*, **117**, 236–248.
- Domine, F., A. Cabanes, A.-S. Taillandier, and L. Legagneux (2001), Specific surface area of snow samples determined by CH₄ adsorption at 77 K, and estimated by optical microscopy and scanning electron microscopy, *Environ. Sci. Technol.*, **35**, 771–780.
- Durand, M., E. J. Kim, and S. A. Margulis (2008), Quantifying uncertainty in modeling snow microwave radiance for a mountain snowpack at the point-scale, including stratigraphic effects, *IEEE Trans. Geosci. Remote Sens.*, **46**(6), 1753–1767.
- Elder, K., D. Cline, G. E. Liston, and R. Armstrong (2009), NASA Cold Land Processes Experiment (CLPX 2002/03): Field measurements of snowpack properties and soil moisture, *J. Hydrometeorol.*, **10**(1), 320–329.
- Fierz, C., R. L. Armstrong, Y. Durand, P. Etchevers, E. Greene, D. M. McClung, K. Nishimura, P. K. Satyawali, and S. A. Sokratov (2009), The International Classification for Seasonal Snow on the Ground. IHP-VII Technical Documents in Hydrology No.83, IACS Contribution No.1, UNESCO-IHP, Paris.
- Fletcher, S. J., G. E. Liston, C. A. Hiemstra, and S. D. Miller (2012), Assimilating MODIS and AMSR-E snow observations in a snow evolution model, *J. Hydrometeorol.*, **13**, 1475–149.
- Freitag, J., F. Wilhelms, and S. Kipfstuhl (2004), Microstructure-dependent densification of polar firn derived from X-ray microtomography, *J. Glaciol.*, **50**(169), 243–250.
- Gallet, J. C., F. Domine, C. S. Zender, and G. Picard (2009), Measurement of the specific surface area of snow using infrared reflectance in an integrating sphere at 1310 and 1550 nm, *The Cryosphere*, **3**(2), 167–182.
- Grenfell, T. C., and S. G. Warren (1999), Representation of a nonspherical ice particle by a collection of independent spheres for scattering and absorption of radiation, *J. Geophys. Res.*, **104**(D24), 31,697–31,709.
- Grody, N. (2008), Relationship between snow parameters and microwave satellite measurements: Theory compared with Advanced Microwave Sounding Unit observations from 23 to 150 GHz, *J. Geophys. Res.*, **113**, D22108, doi:10.1029/2007JD009685.
- Hallikainen, M. T., F. T. Ulaby, M. Dobson, M. El-Rayes, and L.-K. Wu (1985), Microwave dielectric behavior of wet soil—Part I: Empirical models and experimental observations, *IEEE Trans. Geosci. Remote Sens.*, **GE-23**(1), 25–34.
- Hallikainen, M., F. Ulaby, and T. Deventer (1987), Extinction behavior of dry snow in the 18- to 90-GHz range, *IEEE Trans. Geosci. Remote Sens.*, **GE-25**(6), 737–745.
- Harlow, C., and R. Essery (2012), Tundra snow emissivities at MHS frequencies: MEMLS validation using airborne microwave data measured during CLPX-II, *IEEE Trans. Geosci. Remote Sens.*, **50**(11), 4262–4278.
- Heggli, M., B. Köchle, M. Matzl, B. R. Pinzer, F. Riche, S. Steiner, D. Steinfeld, and M. Schneebel (2011), Measuring snow in 3-D using X-ray tomography: Assessment of visualization techniques, *Ann. Glaciol.*, **52**(58), 231–236.
- Homan, J. W., C. H. Luce, J. P. McNamara, and N. F. Glenn (2011), Improvement of distributed snowmelt energy balance modeling with MODIS-based NDSI-derived fractional snow-covered area data, *Hydrol. Processes*, **25**, 650–660.
- Kelly, R. (2009), The AMSR-E snow depth algorithm: Description and initial results, *J. Remote Sens. Soc. Jpn.*, **29**, 307–317.
- Kelly, R., A. Chang, L. Tsang, and J. Foster (2003), A prototype AMSR-E global snow area snow depth algorithm, *IEEE Trans. Geosci. Remote Sens.*, **41**(2), 230–242.
- Kim, M. J. (2006), Single scattering parameters of randomly oriented snow particles at microwave frequencies, *J. Geophys. Res.*, **111**, D14201, doi:10.1029/2005JD006892.
- Kim, E. J., and A. W. England (2003), A yearlong comparison of plot-scale and satellite footprint-scale 19 and 37 GHz brightness of the Alaskan North Slope, *J. Geophys. Res.*, **108**(D13), 4388, doi:10.1029/2002JD002393.
- Kontu, A., and J. Pulliainen (2010), Simulation of spaceborne microwave radiometer measurements of snow cover using in situ data and brightness temperature modeling, *IEEE Trans. Geosci. Remote Sens.*, **48**(3), 1031–1044.
- Kurvonen, L., and M. Hallikainen (1997), Influence of land-cover category on brightness temperature of snow, *IEEE Trans. Geosci. Remote Sens.*, **35**(2), 367–377.
- Langlois, A., A. Royer, B. Montpetit, G. Picard, L. Brucker, L. Arnaud, P. Harvey-Collard, M. Fily, and K. Göta (2010), On the relationship between snow grain morphology and in-situ near infrared calibrated reflectance photographs, *Cold Reg. Sci. Technol.*, **61**(1), 34–42.
- Langlois, A., A. Royer, C. Derksen, B. Montpetit, F. Dupont, and K. Göta (2012), Coupling the snow thermodynamic model SNOWPACK with the microwave emission model of layered snowpacks for subarctic and arctic snow water equivalent retrievals, *Water Resour. Res.*, **48**, W12524, doi:10.1029/2012WR012133.
- Lemmetyinen, J., C. Derksen, J. Pulliainen, W. Strapp, P. Toose, A. Walker, S. Tauriainen, J. Pihlflyckt, J. Kärnä, and M. T. Hallikainen (2009), A comparison of airborne microwave brightness temperatures and snowpack properties across the boreal forests of Finland and Western Canada, *IEEE Trans. Geosci. Remote Sens.*, **47**(3), 965–978.
- Lemmetyinen, J., J. Pulliainen, A. Rees, A. Kontu, Q. Yubao, and C. Derksen (2010), Multiple-layer adaptation of HUT snow emission model: Comparison with experimental data, *IEEE Trans. Geosci. Remote Sens.*, **48**(7), 2781–2794.
- Löwe, H., J. Spiegel, and M. Schneebeli (2011), Interfacial and structural relaxations of snow under isothermal conditions, *J. Glaciol.*, **57**(203), 499–510.
- Marshall, H. P., G. Koh, and M. Sturm (2008), Ultra-broadband portable microwave FMCW radars for measuring snow depth, snow water equivalent, and stratigraphy: Practical considerations. Proceedings of the XXIXth International Union of Radio Science (URSI) General Assembly.
- Matzl, M., and M. Schneebeli (2006), Measuring specific surface area of snow by near-infrared photography, *J. Glaciol.*, **52**(179), 558–564.
- Mätzler, C. (1996), Microwave permittivity of dry snow, *IEEE Trans. Geosci. Remote Sens.*, **34**(2), 573–581.
- Mätzler, C. (2002), Relation between grain-size and correlation length of snow, *J. Glaciol.*, **48**(162), 461–466.

- Mätzler, C., and A. Wiesmann (1999), Extension of the microwave emission model of layered snowpacks to coarse-grained snow, *Remote Sens. Environ.*, 70(3), 317–325.
- Molotch, N. P., and S. A. Margulis (2008), Estimating the distribution of snow water equivalent using remotely sensed snow cover data and a spatially distributed snowmelt model: A multi-resolution, multi-sensor comparison, *Adv. Water Resour.*, 31, 1503–1514.
- Montpetit, B., A. Royer, A. Langlois, P. Cliche, A. Roy, N. Champollion, G. Picard, F. Domine, and R. Obbard (2012), New shortwave infrared albedo measurements for snow specific surface area retrieval, *J. Glaciol.*, 58(11), 941–952.
- Montpetit, B., A. Royer, A. Roy, A. Langlois, and C. Derksen (2013), Snow microwave emission modeling of ice lenses within a snowpack using the Microwave Emission Model for Layered Snowpacks, *IEEE Trans. Geosci. Remote Sens.*, 51(9), 4705–4717.
- Painter, T. H., N. P. Molotch, M. Cassidy, M. Flanner, and K. Steffen (2007), Contact spectroscopy for determination of stratigraphy of snow optical grain size, *J. Glaciol.*, 53(180), 121–127.
- Payne, J. T., A. W. Wood, A. F. Hamlet, R. N. Palmer, and D. P. Lettenmaier (2004), Mitigating the effects of climate change on the water resources of the Columbia River Basin, *Clim. Change*, 62(1–3), 233–256.
- Picard, G., L. Arnaud, F. Domine, and M. Fily (2009), Determining snow specific surface area from near-infrared reflectance measurements: Numerical study of the influence of grain shape, *Cold Reg. Sci. Technol.*, 56(1), 10–17.
- Proksch, M., H. Löwe, and M. Schneebeli (2012), Statistical model for the correlation length of snow derived from Snow-Micro-Pen measurements, *Geophys. Res.*, Abstr. 14 EGU2012: 14125.
- Pulliainen, J. T., J. Grandell, and M. T. Hallikainen (1999), HUT snow emission model and its applicability to snow water equivalent retrieval, *IEEE Trans. Geosci. Remote Sens.*, 37(3), 1378–1390.
- Rees, A., J. Lemmetyinen, C. Derksen, J. Pulliainen, and M. English (2010), Observed and modelled effects of ice lens formation on passive microwave brightness temperatures over snow covered tundra, *Remote Sens. Environ.*, 114(1), 116–126.
- Roy, V., K. Goita, A. Royer, A. E. Walker, and B. E. Goodison (2004), Snow water equivalent retrieval in a Canadian boreal environment from microwave measurements using the HUT snow emission model, *IEEE Trans. Geosci. Remote Sens.*, 42(9), 1850–1859.
- Roy, A., G. Picard, A. Royer, B. Montpetit, F. Dupont, A. Langlois, C. Derksen, and N. Champollion (2013), Brightness temperature simulations of the Canadian seasonal snowpack driven by measurements of the snow specific surface area, *IEEE Trans. Geosci. Remote Sens.*, 99, 1–13.
- Rutter, N., D. Cline, and L. Li (2008), Evaluation of the NOHRSC snow model (NSM) in a one-dimensional mode, *J. Hydrometeorol.*, 9(4), 695–711.
- Schneebeli, M. (2004), Numerical simulation of elastic stress in the microstructure of snow, *Ann. Glaciol.*, 38, 339–342.
- Sturm, M., and C. Benson (2004), Scales of spatial heterogeneity for perennial and seasonal snow layers, *Ann. Glaciol.*, 38, 253–260.
- Takala, M., K. Luojus, J. Pulliainen, C. Derksen, J. Lemmetyinen, J.-P. Kärnä, J. Koskinen, and B. Bojkov (2011), Estimating northern hemisphere snow water equivalent for climate research through assimilation of space-borne radiometer data and ground-based measurements, *Remote Sens. Environ.*, 115(12), 3517–3529.
- Tape, K. D., N. Rutter, H. P. Marshall, R. Essery, and M. Sturm (2010), Recording microscale variations in snowpack layering using near-infrared photography, *J. Glaciol.*, 56(195), 75–80.
- Tedesco, M., R. E. J. Kelly, J. L. Foster, and A. T. C. Chang (2004), *AMSR-E/Aqua Daily L3 Global Snow Water Equivalent EASE-Grids V002*, National Snow and Ice Data Center: Digital media, Boulder, Colo.
- Tedesco, M., E. J. Kim, A. Gasiewski, M. Klein, and B. Stankov (2005), Analysis of multiscale radiometric data collected during the Cold Land Processes Experiment-1 (CLPX-1), *Geophys. Res. Lett.*, 32, L18501, doi:10.1029/2005GL023006.
- Tedesco, M., E. J. Kim, D. Cline, T. Graf, T. Koike, R. Armstrong, M. J. Brodzik, and J. Hardy (2006), Comparison of local scale measured and modelled brightness temperatures and snow parameters from the CLPX 2003 by means of a dense medium radiative transfer theory model, *Hydrol. Processes*, 20(4), 657–672.
- Toure, A. M., K. Goita, A. Royer, C. Mätzler, and M. Schneebeli (2008), Near-infrared digital photography to estimate snow correlation length for microwave emission modeling, *Appl. Opt.*, 47(36), 6723–6733.
- Tsang, L., K.-H. Ding, S. Huang, and X. Xu (2013), Electromagnetic computation in scattering of electromagnetic waves by random rough surface and dense media in microwave remote sensing of land surfaces, *Proc. IEEE*, 101(2), 255–279.
- Wiesmann, A., and C. Mätzler (1999), Microwave emission model of layered snowpacks, *Remote Sens. Environ.*, 70(3), 307–316.
- Yang, D. Q., et al. (1999), Quantification of precipitation measurement discontinuity induced by wind shields on national gauges, *Water Resour. Res.*, 35(2), 491–508.
- Zhang, L., J. Shi, Z. Zhang, and K. Zhao (2003), The estimation of dielectric constant of frozen soil-water mixture at microwave bands, *IEEE Int. Geosci. Remote Sens. Symp.*, 4, 2903–2905.